Experimental x-ray-production cross sections for the M_3, M_4, and M_5 subshells of Pt and Au by electron impact

Alejo Carreras, Gustavo Castellano, Silvina Segui,* and Jorge Trincavelli†
Instituto de Física Enrique Gaviola (IFEG-CONICET), Facultad de Matemática, Astronomía, Física y Computación (FaMAF), Universidad Nacional de Córdoba, Córdoba, Argentina

(Received 16 April 2020; accepted 1 July 2020; published 27 July 2020)

X-ray-production cross sections for M_3, M_4, and M_5 subshells of Pt and Au by electron impact were experimentally determined at incident energies ranging between 2.8 and 28 keV. To this purpose, Pt and Au thick targets were irradiated by an electron beam in a field-emission-gun scanning electron microscope, and the x-ray-emission spectra were recorded with an energy-dispersive spectrometer. The x-ray-production cross sections were obtained as a result of the spectral processing performed through a careful parameter optimization routine previously developed, which involves an analytical function for the prediction of the experimental spectra, on the basis of ionization depth distribution functions. The results are compared with the scarce data available in the literature.

DOI: 10.1103/PhysRevA.102.012817

I. INTRODUCTION

The interest in ionization-relaxation processes is widely spread in the field of atomic physics and also in the frame of different materials characterization techniques based on x-ray-emission atomic spectroscopy. Particularly, an accurate knowledge of ionization cross sections by electron impact is crucial for Monte Carlo simulation of electron and photon transport in matter [1], for chemical quantification by means of electron probe microanalysis [2] or Auger spectroscopy [3], and for applications in radiotherapy [4]. In the case of heavy elements, reliable data of M-shell ionization cross sections are especially important, since among the possible ionizations these are the most useful in the low-energy regime, compatible with many materials characterization techniques.

After several classical approaches (e.g., Ref. [5]), many quantum-mechanical calculations of ionization cross sections have been performed by using the relativistic plane-wave Born approximation (PWBA), introducing different approximations in order to simplify the assessments. This approach was implemented by Scofield [6], who provided a parametrization for projectile energies E_o well above the ionization threshold E_c, typically for overvoltages $U = E_o/E_c$ greater that 20. More recently, a parametrization extended PWBA for lower energies, this generalization being appropriate for $U > 16$ [7]. For projectile energies closer to E_c, the target-atom electrostatic field distorts the wave associated with the incident electron, requiring a more realistic approach. To this end, in the distorted-wave Born approximation (DWBA), the incoming and scattered electron wave functions include the distortion caused by the atomic field, allowing for the description of exchange effects in a consistent way [8]. An analytical parametrization was provided for this more realistic model, which is valid for $U < 16$ down to energies close to the binding energy [7].

Unfortunately, experimental determinations of x-ray-production cross sections are very scarce, and therefore it is not easy to support the theoretical estimates of ionization cross sections provided by DWBA in the energy range close to the ionization threshold, where the PWBA approach is expected to fail. This is precisely the energy range of interest for the materials characterization techniques based on x-ray-emission or Auger-electron spectroscopy. As pointed out by Merlet *et al.* [9], the scarce measurements of M-shell x-ray production cross sections found in the literature were mostly performed at very-high-incident electron energies [10,11] or were mainly focused on the energy dependence of the cross section [12–14]. Nevertheless, absolute experimental determinations were recently carried out in the low-overvoltage range for Au, Bi [9], Pb [15], Th [16], and U [17]. All these measurements were performed on thin targets, which permits a direct evaluation of the x-ray-production cross section, as long as an accurate knowledge of the target thickness can be ensured.

To avoid the experimental difficulties for furnishing such thin samples and to overcome the uncertainties introduced by the backscattered contribution produced in the supporting substrate, a thick target method can also be implemented [18]. This approach has the additional advantage of being suitable in low-statistics experiments, such as the determination of multiple-ionization cross sections [19]. However, this thick-target method relies on certain assumptions that are not always suitable, particularly in the case of heavy elements; e.g., electron trajectories are assumed to be linear within the sample and backscattering losses are not taken into account.

In this work, x-ray-production cross sections for M_3, M_4, and M_5 subshells of Pt and Au by electron incidence were

*On leave from Centro Atómico Bariloche (CNEA), Av. Bustillo 9500, 8400 S. C. de Bariloche, Argentina.
†trincavelli@famaf.unc.edu.ar

experimentally determined through an alternative approach also based on thick targets. To this purpose, x-ray spectra induced by keV-electron impact were measured at different beam energies with an energy-dispersive detector. These spectra were then processed by means of a robust optimization procedure implemented in a previous work [20] and successfully used for the determination of different atomic parameters [21–25]. In this approach, the values for the x-ray-production cross sections were assessed from the prediction of characteristic spectra on the basis of ionization depth distribution functions [26], and therefore no simplifications were required regarding either the electron trajectories within the material or backscattering losses.

II. EXPERIMENTAL

Platinum and gold x-ray-emission spectra were obtained from pure thick standards (Micro-Analysis Consultants, Ltd.). The possible influence of impurities was opportunely evaluated, and according to the levels informed by the manufacturer, they can be neglected for the purposes of the present work. These finely polished standards are grouped together in a single brass block. The mounting medium for this assembly is a nonconductive resin, so that carbon coating is required to ensure good conductivity from the metal standard to the brass mount which encloses the resin.

The Pt and Au samples were irradiated by an electron beam in a Carl Zeiss Σigma field-emission scanning electron microscope. As mentioned above, the x-ray spectra were recorded using an energy-dispersive spectrometer (EDS) attached to the microscope. This kind of spectrometer is much faster than the wavelength-dispersive ones, and its resolution is good enough for the problem faced in this work. The EDS used consists of an Oxford silicon drift detector with an Aztec characterization system. The detector front window is an ultrathin polymer layer supported by a 380-μm-thick silicon structure with 77% open area.

The nominal incident energies used ranged from 2.8 to 28 keV, with beam currents between 100 and 1400 pA, and acquisition live times between 120 and 420 s, suitable to achieve good statistics in all cases. As an example, Fig. 1 shows the spectrum corresponding to Pt irradiated at 10 keV.

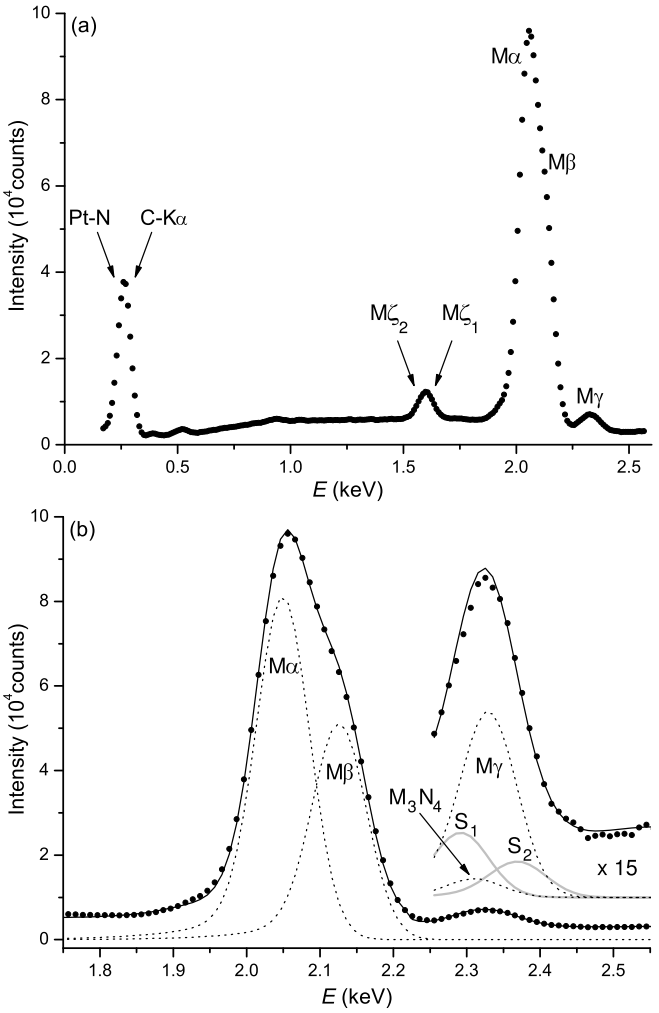

FIG. 1. X-ray spectrum of Pt irradiated with 10 keV electrons. (a) Whole experimental spectrum showing platinum M and N lines and the carbon-$K\alpha$ peak corresponding to the conductive coating. (b) Detailed view of the $M\alpha$, $M\beta$, and $M\gamma$ peaks along with the obtained fit. Dots, experimental data; solid black line, fit; dotted lines, individual contribution of diagram transitions; solid gray lines, S_1 and S_2 sum peaks (see text). The inset shows a magnified view of the $M\gamma$ region.

III. METHODOLOGY

The x-ray-production cross sections were obtained from the experimental data, by using a spectral processing tool previously developed and implemented in the software POEMA [20]. In order to appropriately fit an experimental spectrum, it is necessary to describe it by means of a realistic analytical function, which depends on several adjustable parameters, including the sought magnitudes. Thus, the x-ray-production cross sections are determined as a result of the optimization procedure. In this section, the spectral processing tool and the optimization strategy are briefly detailed.

A. Spectral processing

The parameter optimization method involves the minimization of the quadratic differences between the experimental spectrum and the analytical function proposed to describe it:

$$\chi^2 = \frac{1}{N_c - N_p} \sum_{i=1}^{N_c} \frac{(\tilde{I}_i - I_i)^2}{\tilde{I}_i},$$

where N_c is the number of channels, N_p is the number of parameters to be refined, and I_i and $\tilde{I}_i$ are respectively the experimental and analytical x-ray intensities for channel i.

The estimate provided for $\tilde{I}_i$ is a function of the energy E_i:

$$\tilde{I}_i = B(E_i) + \sum_q P_q S_q(E_i), \tag{1}$$

where B is the background radiation [27], S_q is a function accounting for the peak shape, i.e., a Gaussian function corrected by peak asymmetry (see Sec. III A 2), and P_q is the intensity of the characteristic q line, given by (see the

Appendix):

$$P_q = N_e \sigma_\ell^x \, p_q (ZAF)_q \, \varepsilon(E_q), \tag{2}$$

where N_e is the number of incident electrons; σ_ℓ^x is the x-ray production cross section for the ℓ subshell, i.e., the product of the final vacancy production cross section $\tilde{\sigma}_\ell$ evaluated at the energy of the incident electrons E_o, and the fluorescence yield ω_ℓ; p_q and E_q are the relative transition probability and the characteristic energy of the q line, respectively; Z, A, and F are related to the so-called atomic number, absorption, and fluorescence correction factors, respectively [28]; and ε is the spectrometer efficiency.

The global refinable parameters are a scale factor involved in the bremsstrahlung description and parameters related to the spectrometer calibration and instrumental broadening. On the other hand, individual parameters associated with each diagram line, such as the characteristic energy, the relative transition probability, the natural linewidth, etc., can also be refined through the optimization routine [20]. Finally, the x-ray-production cross sections can be obtained for each atomic shell from the optimization of the σ_ℓ^x parameters in Eq. (2). Some features of the spectral processing, such as the detection efficiency, the peak asymmetry, and the influence of the carbon coating over the used standards, were faced with special care and require a detailed discussion.

1. Detection efficiency

The efficiency of the x-ray detector ε is defined as the fraction of photons emitted by the sample that are registered by the detector, and it can be expressed as the product of the intrinsic efficiency ε' and the solid angle fraction $\frac{\Delta\Omega}{4\pi}$ subtended by the detector from the beam impact point on the sample surface:

$$\varepsilon = \varepsilon' \frac{\Delta\Omega}{4\pi},$$

where the intrinsic efficiency ε' is a function of the photon energy and represents the fraction of photons arriving at the detector that are indeed registered.

(a) Intrinsic efficiency. The model described in Ref. [29] was considered for the intrinsic efficiency

$$\varepsilon' = (0.77 + 0.23\, e^{-\mu_g \rho_g x_g}) e^{-\mu_w \rho_w x_w} (1 - e^{-\mu_d \rho_d x_d}), \tag{3}$$

where the subindices g, w, and d respectively denote the supporting silicon grid, the front window, and the active detection layer; μ stands for the mass attenuation coefficient; ρ is the mass density; and x represents the thickness corresponding to each layer.

The first factor in Eq. (3) corresponds to the fraction of photons that pass through the supporting grid, and it was evaluated using the parameters specified by the manufacturer: an open area fraction of 0.77 and a grid thickness of 380 μm [30].

The second factor represents the probability of crossing the detector window and was previously determined by measuring and fitting a set of spectra from standard mineral samples, with particular care in the low-energy region. Although the detector window consists of a complex structure of different layers, in the photon energy range of interest, it is a good approximation to consider a single layer with the nominal window composition, i.e., 69% C, 3% H, 21% O, and 7% N mass concentrations, with a density of 1.4 g/cm^3, as provided by the manufacturer [29], and the corresponding effective thickness x_w. The latter was determined by fitting the spectra mentioned above with POEMA, optimizing x_w along with a background scale factor. The value $x_w = 490$ nm was obtained with this procedure.

The third factor is the fraction of photons that do not escape from the active detector region. Since the detector's active layer thickness comprises a few millimeters, this factor can be neglected (i.e., considered equal to unity) for the energies involved in the present work.

(b) Solid angle. To determine the solid angle subtended by the detector, the front collimator area and its distance to the beam impact point in the sample surface were measured using photographs taken within the microscope specimen chamber to avoid touching the detector's window. In fact, this measured area corresponds to the front section presented by the collimator, since the detector's effective area is not accessible. Therefore, the solid angle $(\Delta\Omega)_c$ measurement provides an upper bound for the real solid angle $\Delta\Omega$:

$$\Delta\Omega = k \times (\Delta\Omega)_c, \tag{4}$$

where k is a scale factor lower than unity. This factor was determined from K-shell x-ray-production cross sections σ_{ref}^x accurately known for different atomic numbers. To this end, K spectra were measured from pure Al, Ni, and Cu standards, at beam energies of 6, 8, and 10 keV for Al; 12 and 15 keV for Ni; and 25 keV for Cu. From these spectra, the σ_K^x x-ray-production cross sections were obtained as explained above, except for the sought k factor, so that

$$k = \frac{\sigma_K^x}{\sigma_{\text{ref}}^x}.$$

The values for σ_{ref}^x were taken from Ref. [7] and are theoretical predictions accurately describing the experimental data available [31]. After averaging the six values obtained for the scale factor, the resulting value was $k = 0.74 \pm 0.03$. Taking into account that the experimental determination of the geometry involved produced $(\Delta\Omega)_c/(4\pi) = 0.0033$, the effective solid angle fraction subtended by the detector resulted in $\Delta\Omega/(4\pi) = 0.0024 \pm 0.0001$.

2. Peak asymmetry

The characteristic peaks recorded by an energy dispersive spectrometer are slightly distorted due to incomplete charge collection effects within the detector. This effect produces a tail towards the low-energy region of the peak. This asymmetric contribution is described by an exponential tail convoluted with a Gaussian function accounting for the instrumental broadening [32]:

$$T_q(E_i) = t_q \frac{e^{w_q^2/(2\beta_q^2)}}{2\beta_q} e^{(E_i - E_q)/\beta_q} \operatorname{erfc}\left(\frac{E_i - E_q}{\sqrt{2} w_q} + \frac{w_q}{\sqrt{2}\beta_q} \right),$$

where w_q denotes the instrumental width and the asymmetric shape is characterized by two parameters: the relative amplitude t_q and the broadening β_q, which depend on the photon energy and can be refined along the optimization process.

Thus, the characteristic peak profile can be expressed as

$$S_q(E_i) = M[G_q(E_i) + T_q(E_i)], \tag{5}$$

where M is a normalization factor defined so that the integral of $S_q(E_i)$ is equal to 1. To determine the parameters t_q and β_q, several spectra were acquired from pure and mineral standards bearing intense characteristic peaks with energies close to the Pt and Au M lines analyzed here. To this end, these spectra were processed by means of the optimization routine described above.

3. Carbon coating

As mentioned in Sec. II, the pure standard set mount is coated by a thin carbon layer in order to provide good conductivity. Since this coating modifies the transport of the incident electrons and emerging photons, it is necessary to determine the carbon layer's thickness to assess its influence on the measured spectra. To this end, spectra were measured irradiating a region of the brass block close to the standards used here. A thickness of 62.5 ± 1.0 nm was obtained from the spectral fit performed by means of the software POEMA.

It is important to point out that Eqs. (1) and (2) involve the number of incident electrons effectively reaching the standards analyzed after traversing this carbon coating. For this reason, it must be borne in mind that some fraction of the incident beam is lost. The transmitted electrons have an energy distribution dN_t/dE, and their average incident angle when reaching the metal surface is modified. Even though these effects are already considered in the software used [33], the energy loss is not sufficiently well described when the beam energy is close to the binding energy of interest E_ℓ. In order to find the effective energy of the electrons when reaching the Pt or Au standard surface covered by the carbon layer, a first estimate was obtained by assessing the Duane-Hunt limit E_{DH} in the experimental spectra [34]. This value was determined from each experimental spectrum as the energy for which the spectral curve equals 0, and it is a good measure of the incident electron energy. The energy distribution of the electrons transmitted through the carbon layer was then studied by means of Monte Carlo simulations. To this end, the PENCYL main program distributed with the PENELOPE package [1] was used to simulate electron beams of energies E_{DH} impinging on an isolated carbon layer of 62.5 nm. From the resulting transmitted electron energy distributions dN_t/dE, for each E_{DH}, the effective energy E_o^ℓ and the number of electrons reaching the target N_ℓ with energy above the absorption edge E_ℓ were assessed as follows:

$$E_o^\ell = \frac{1}{N_\ell}\int_{E_\ell}^{E_{\mathrm{DH}}} E\,\frac{dN_t}{dE}dE,$$
$$N_\ell = \int_{E_\ell}^{E_{\mathrm{DH}}} \frac{dN_t}{dE}dE. \tag{6}$$

These effective energies and numbers of transmitted electrons were respectively used instead of E_o and N_e in Eq. (2), the former magnitude being used to assess the ZAF factors. Figure 2 presents the energy distribution of the transmitted electrons impinging with $E_{\mathrm{DH}} = 3.83$ keV as an example.

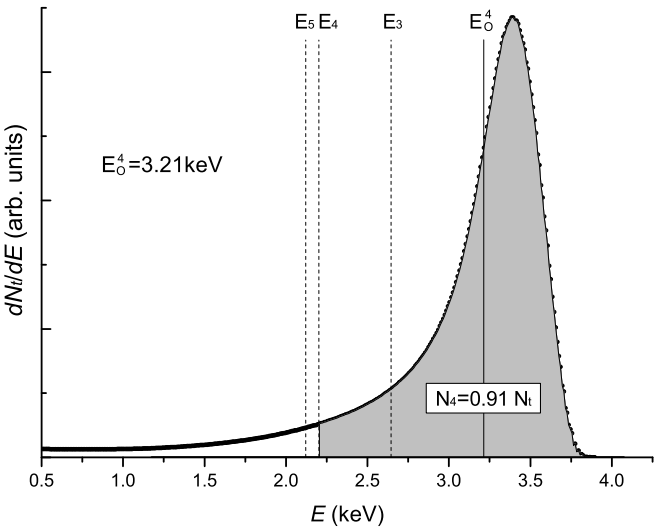

FIG. 2. Energy distribution of 3.83-keV electrons after crossing a carbon foil of 62.5 nm. The dashed lines indicate the E_3, E_4, and E_5 absorption edges of Pt. The effective energy E_o^4 corresponding to the Pt M_4 subshell and the number of electrons N_4 reaching the target with energy above the E_4 absorption edge are also shown.

B. Optimization strategy

To obtain the x-ray-production cross sections, the Pt and Au spectra were processed using the software POEMA following a cautious strategy to avoid local minima. In general terms, the spectral fitting procedure consisted of the sequential refinement of the following:

(i) instrumental parameters: peak broadening and calibration parameters, in a wide spectral region including all the characteristic peaks present in the spectra, and

(ii) parameters related to the peak intensities: the x-ray-production cross sections σ_ℓ^x and a background scale factor, in a region around the peaks of interest.

The characteristic energies E_q and the relative transition probabilities p_q were determined in a previous work [35], although in the cases of resolved peaks with good statistics it was possible to refine the p_q parameters here. Regarding detection efficiency, peak asymmetry, and influence of the carbon coating, the corresponding parameters were obtained as mentioned in Sec. III A.

Concerning the x-ray-production cross sections, they were determined in two stages considering different spectral regions. In a first stage, the M_4 and M_5 energy range was selected as the region of interest. First, σ_5^x was determined by means of the refinement of the parameters σ_4^x and σ_5^x and the background scale factor, setting the effective energy E_o^5 and number of electrons N_5 assessed by Monte Carlo simulations. Thus, the σ_4^x parameter lacks physical meaning, merely allowing for a good spectral description, while the σ_5^x value obtained is an appropriate result for the corresponding x-ray-production cross section. Then, an analogous procedure was followed to obtain σ_4^x, refining again σ_4^x and σ_5^x and the background factor in the same spectral region, but setting E_o^4 and N_4 according to the Monte Carlo results.

In a second stage, the spectral region corresponding to the M_3 peak was considered for the determination of σ_3^x. In

TABLE I. X-ray-production cross sections for platinum. The tabulated energies correspond to E_o^ℓ calculated according to Eq. (6).

E_o^3 (keV)	σ_3^x (b)	E_o^4 (keV)	σ_4^x (b)	E_o^5 (keV)	σ_5^x (b)
–	–	2.30(5)	64(4)	2.25(6)	107(6)
–	–	2.40(6)	120(9)	2.36(7)	200(20)
2.87(7)	18(5)	2.74(9)	280(10)	2.72(9)	450(20)
3.28(7)	20(2)	3.21(8)	400(20)	3.20(8)	610(30)
3.79(5)	22(2)	3.75(5)	470(20)	3.75(5)	690(30)
4.34(6)	30(3)	4.32(6)	500(20)	4.32(7)	720(30)
5.42(7)	36(3)	5.41(7)	530(30)	5.41(7)	760(40)
6.488(6)	43(3)	6.482(5)	540(30)	6.481(5)	770(30)
7.545(5)	40(3)	7.540(5)	510(20)	7.539(5)	710(30)
8.618(5)	42(2)	8.613(5)	490(20)	8.613(5)	670(30)
9.61(2)	45(3)	9.60(2)	490(20)	9.60(2)	680(30)
11.67(2)	41(3)	11.67(2)	450(20)	11.67(2)	620(30)
14.68(3)	37(3)	14.67(3)	410(20)	14.67(3)	560(30)
19.71(5)	30(2)	19.71(2)	340(20)	19.71(2)	460(20)
27.74(8)	23(3)	27.74(9)	250(20)	27.74(8)	350(20)

TABLE II. X-ray-production cross sections for gold. The tabulated energies correspond to E_o^ℓ calculated according to Eq. (6).

E_o^3 (keV)	σ_3^x (b)	E_o^4 (keV)	σ_4^x (b)	E_o^5 (keV)	σ_5^x (b)
–	–	2.36(5)	30(3)	2.29(6)	80(9)
–	–	2.5(1)	90(7)	2.5(1)	180(20)
–	–	2.8(2)	200(10)	2.8(2)	360(20)
3.1(1)	13(2)	3.0(2)	230(10)	3.0(2)	410(20)
3.3(1)	20(3)	3.3(1)	320(30)	3.3(1)	550(40)
3.7(2)	22(3)	3.6(2)	320(40)	3.6(2)	540(50)
3.8(1)	27(3)	3.8(1)	400(20)	3.8(1)	650(30)
4.1(1)	25(2)	4.1(1)	380(20)	4.1(1)	640(30)
4.34(7)	33(3)	4.34(7)	450(20)	4.32(7)	740(30)
5.39(5)	43(3)	5.38(5)	510(20)	5.38(5)	810(40)
6.479(6)	45(3)	6.473(5)	520(30)	6.472(6)	820(40)
7.546(5)	49(3)	7.541(6)	510(20)	7.540(6)	800(20)
8.615(6)	46(3)	8.610(6)	490(20)	8.608(5)	770(40)
9.671(6)	47(3)	9.666(6)	480(20)	9.665(5)	740(30)
11.68(1)	45(3)	11.67(1)	450(20)	11.67(2)	680(30)
14.71(9)	43(3)	14.71(9)	410(20)	14.70(9)	630(30)
19.81(9)	36(3)	19.81(9)	350(20)	19.81(9)	530(30)
27.7(1)	26(2)	27.7(1)	260(20)	27.7(1)	420(20)

this region, besides the $M\gamma$ and M_3N_4 lines, associated with decays to the M_3 subshell, two sum peaks also appear for each studied element (Au or Pt): they are labeled as S_1 and S_2 in Fig. 1 and respectively correspond to the combination of C-$K\alpha$ photons, emitted from the conductive coating, with the $M\alpha$ and $M\beta$ lines. In fact, the low-energy parent peak also includes the $N_5N_{6,7}$ and N_4N_6 lines arising from the standard.

The sum peaks were taken into account to avoid an overestimation of the M_3 intensity, their energy being fitted accounting for the mentioned different contributions of the parent peaks. The S_1/S_2 intensity ratio was set equal to the obtained $M\alpha/M\beta$ intensity ratio, because the sum peak area is proportional to the product of the corresponding parent peak areas [36]. Finally, the x-ray-production cross section σ_3^x was obtained, after the joint optimization of σ_3^x and the background factor, along with one scale factor that fits the sum peak intensities, setting the effective energy E_o^3 and the number of electrons N_3 obtained from the simulations.

Although these sum peaks must be considered for the assessment of σ_3^x, their contributions were ignored in the determination of σ_4^x and σ_5^x, since their intensities are negligible in comparison to those of the $M\alpha$ and $M\beta$ lines.

IV. RESULTS AND DISCUSSION

A. Results

Tables I and II present the x-ray production cross section values obtained for the M_3, M_4, and M_5 subshells of Pt and Au, respectively. It must be noticed that very scarce experimental data are available in the literature for the magnitudes studied here; in particular, only data for Au σ_5^x have been previously reported.

The uncertainties associated with the x-ray production cross sections were estimated by propagation of the errors corresponding to the beam current, to the detector solid angle given in Eq. (4) (see Sec. III A 1), and to the M-peak intensities obtained from the spectral fitting, whose uncertainties were assessed by propagating the errors in the experimental intensities I_i, carried out through numerical differentiation [37].

To estimate the errors in the tabulated energies, two determinations of the Duane-Hunt limit E_{DH} were performed in each spectrum using two different fitting criteria. From these values, the corresponding effective energies E_o^ℓ were determined by Monte Carlo simulations for each atomic subshell studied. Finally, the error of each energy was estimated as the semidifference between these two effective energies.

B. Comparison to other data

Figures 3 and 4 show the results presented in Tables I and II, along with data from other sources. To compare with theoretical data derived from the ionization cross sections σ_ℓ, it is necessary to rely on several relaxation parameters known with poor precision, namely, the fluorescence yields ω_ℓ and the Coster-Kronig transition probabilities f_{ij} from M_j to M_i subshells. As mentioned in Sec. III A, the x-ray-production cross sections σ_ℓ^x can be related to the final vacancy production cross sections $\tilde{\sigma}_\ell$ by $\sigma_\ell^x = \tilde{\sigma}_\ell\omega_\ell$, where $\tilde{\sigma}_\ell$ can be expressed in terms of σ_ℓ as follows:

$$\begin{aligned}
\tilde{\sigma}_1 &= \sigma_1,\\
\tilde{\sigma}_2 &= \sigma_2 + f_{12}\tilde{\sigma}_1,\\
\tilde{\sigma}_3 &= \sigma_3 + f_{13}\tilde{\sigma}_1 + f_{23}\tilde{\sigma}_2,\\
\tilde{\sigma}_4 &= \sigma_4 + f_{14}\tilde{\sigma}_1 + f_{24}\tilde{\sigma}_2 + f_{34}\tilde{\sigma}_3,\\
\tilde{\sigma}_5 &= \sigma_5 + f_{15}\tilde{\sigma}_1 + f_{25}\tilde{\sigma}_2 + f_{35}\tilde{\sigma}_3 + f_{45}\tilde{\sigma}_4.
\end{aligned}$$

For beam energies above the ionization threshold of the L_i subshells, vacancies can be produced in these levels and decays from M_ℓ to L_i must be considered. Therefore, in these cases further terms must be added to each of the previous

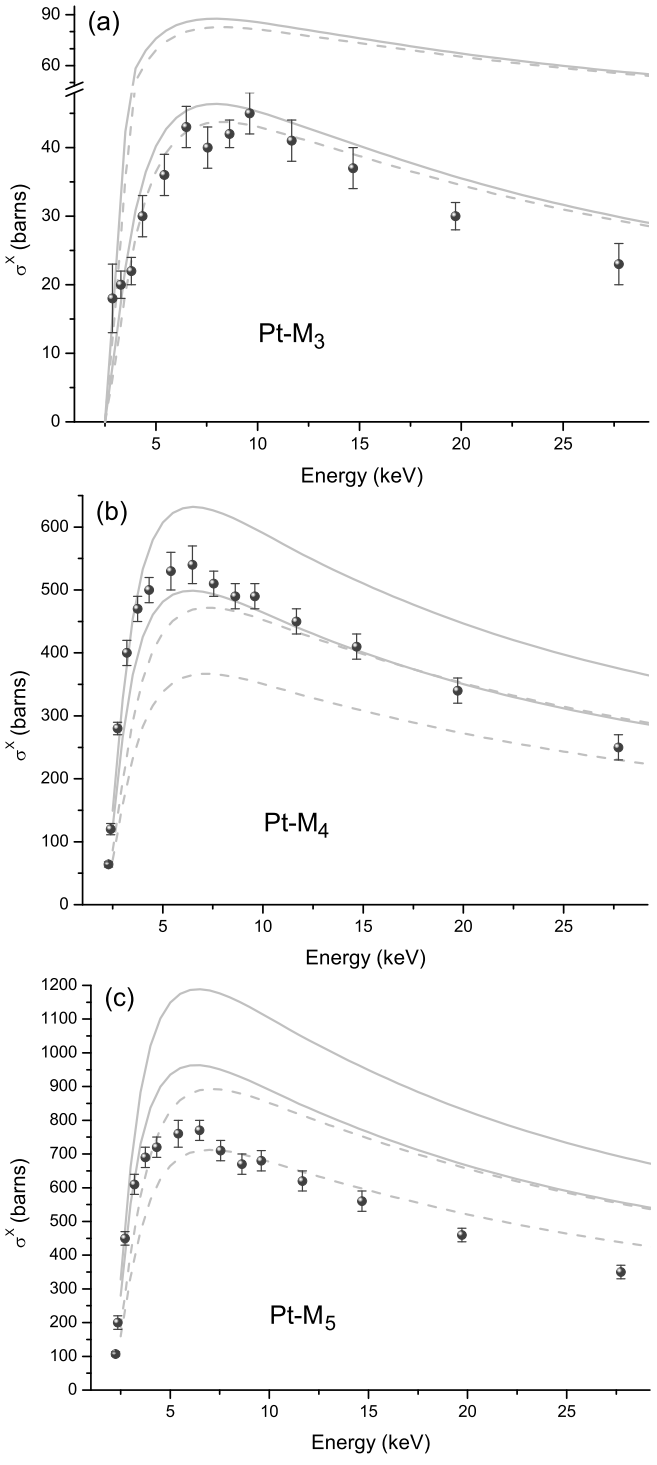

FIG. 3. Platinum x-ray-production cross sections: (a) M_3 subshell, (b) M_4 subshell, and (c) M_5 subshell. Solid spheres represent the present data. The gray lines delimitate regions where results for σ^x derived from theoretical or empirical data for ionization cross sections σ can be obtained when different combinations of relaxation parameters are used. Solid lines are data obtained from Bote and Salvat [45], and dashed lines are data from Casnati *et al.* [46].

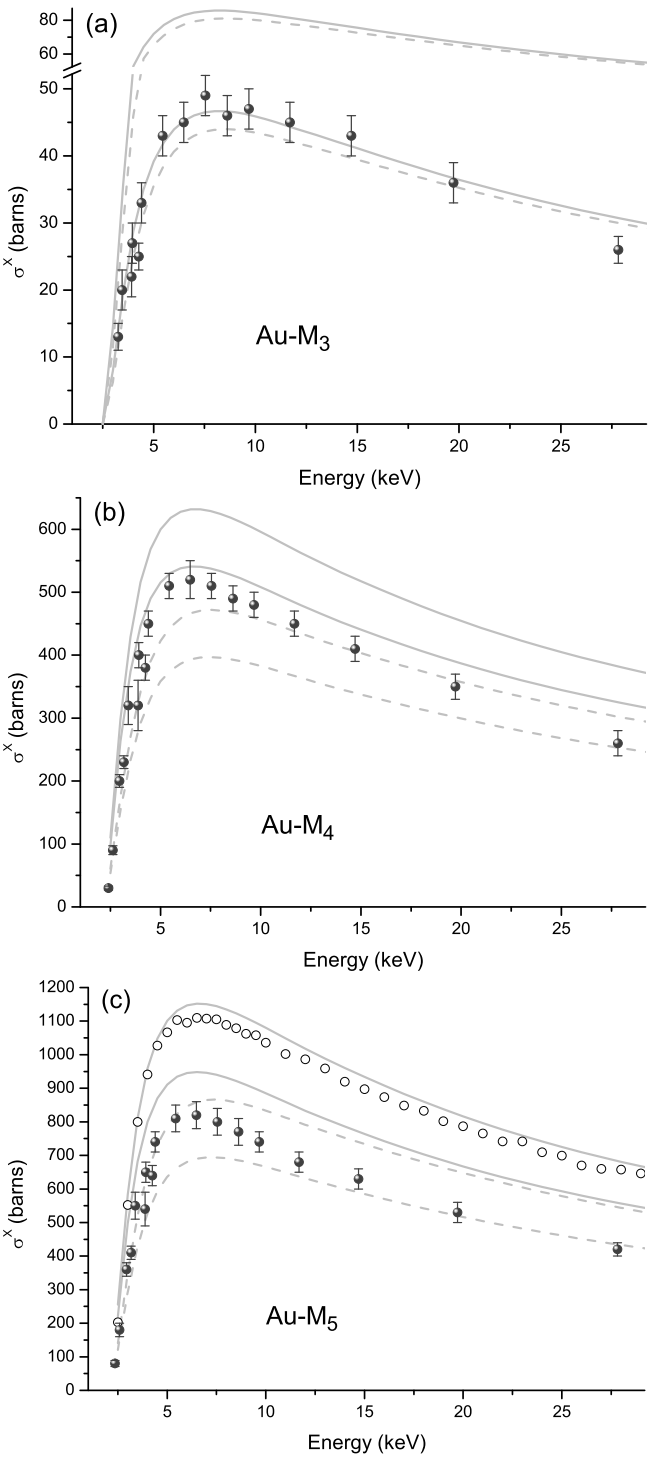

FIG. 4. Gold x-ray-production cross sections: (a) M_3 subshell, (b) M_4 subshell, and (c) M_5 subshell. Solid spheres represent the present data. Empty circles represent the experimental data from Merlet *et al.* [9]. The gray lines delimitate regions where results for σ^x derived from theoretical or empirical data for ionization cross sections σ can be obtained when different combinations of relaxation parameters are used. Solid lines represent data obtained from Bote and Salvat [45], and dashed lines represent data from Casnati *et al* [46].

TABLE III. Coster-Kronig coefficients and fluorescence yields used for comparison.

Element	Ref.	ω_{M_3}	ω_{M_4}	ω_{M_5}	f_{45}	S_{12}	S_{13}	S_{14}	S_{15}	S_{23}	S_{24}	S_{25}	S_{34}	S_{35}
Pt	[38]	0.00729	0.0274	0.0280	0.0798	0.1269	0.5934	0.0772	0.1095	0.0879	0.5762	0.0912	0.0670	0.6112
Pt	[43]	0.00388	0.0226	0.0239	0.077	0.178	0.573	0.069	0.118	0.119	0.671	0.095	0.116	0.785
Au	[38]	0.00764	0.0297	0.0298	0.0664	0.1254	0.5946	0.0775	0.1089	0.0877	0.5757	0.0916	0.0708	0.6042
Au	[43]	0.00419	0.0263	0.0253	0.047	0.156	0.594	0.067	0.113	0.113	0.675	0.094	0.119	0.777

expressions, which can be written as

$$\sigma_{L_1} n_{L_1 M_\ell} + \sigma_{L_2} n_{L_2 M_\ell} + \sigma_{L_3} n_{L_3 M_\ell},$$

where $n_{L_i M_\ell}$ denotes the transition probability from M_ℓ to L_i subshells. For the beam energy range involved here, K vacancies are not created.

Fluorescence yields and Coster-Kronig coefficients are rather difficult to measure, and certain discrepancies arise among the data published in the literature. In this work, values for ω_ℓ [38,39] and f_{ij} [38–44] reported by different authors were taken into account to perform the comparisons. For each σ_ℓ curve chosen to obtain the corresponding σ_ℓ^x values, upper and lower bounds were found by combining the different possible choices for ω_ℓ and f_{ij}. In Figs. 3 and 4, these bounds are shown associated with the theoretical model proposed by Bote and Salvat [45] and with the empirical fit proposed by Casnati *et al.* [46]. The upper bound corresponds to the combination of ω_ℓ given by Perkins *et al.* [38] with the f_{ij} fitted by Kaur and Mittal [43] to McGuire's data [44], while the lower bound is produced by selecting the ω_ℓ values fitted by Kaur and Mittal [43] to McGuire's data [44] with the f_{ij} coefficients reported by Perkins *et al.* [38]. Table III shows the values of the parameters used.

As can be seen from Figs. 3 and 4, there is a noticeable difference between the two predictions used for comparison, especially for M_4 and M_5 subshells. In addition, an important discrepancy arises from the choice of different sets of relaxation parameters for the three subshells studied. Therefore, the choice for the relaxation parameters is crucial for the assessment of σ_ℓ^x from the ionization cross sections σ_ℓ, which is reflected by the large range of values allowed between the abovementioned bounds, particularly, for the M_3 subshell. In this context, the results obtained here are in good agreement with the available predictions. In the case of the M_5 subshell, the present results are closer to the semiempirical approach by Casnati *et al.* [46].

For the specific case of Au M_5, experimental results have been published by Merlet *et al.* [9] and are also shown in Fig. 4(c). A very good agreement was obtained between their data and the theoretical model reported by Bote and Salvat [45], particularly with the relaxation coefficients chosen by the authors (ω_ℓ and f_{ij} from Ref. [38]). Since these experimental data were measured by using gold thin targets, the error in the film thickness determination propagates directly to the obtained cross sections; to determine the film thickness, intensity ratios were measured for a Au film deposited on a Ta substrate for different beam energies. The film thickness was obtained by fitting these intensity ratios using an analytical x-ray-emission model [47] (improved later, see Ref. [48]), which is based on a particular approach for the ionization depth distribution function $\varphi(\rho z)$ [49].

On the other hand, the method presented here is based on the measurement of x-ray intensities produced in thick targets and involves corrections that also rely on an adequate knowledge of the $\varphi(\rho z)$ function. Thus, both methods, the thin target approach implemented by Merlet *et al.* [49] and the present thick target method, depend on the approach chosen to account for the ionization distribution function. It is therefore clear that important efforts should be devoted to complete a reliable experimental data set for this function, in a wide range of elements and beam energies, in order to support new experimental determinations of σ^x.

V. CONCLUSION

This work provides experimental data for the x-ray-production cross sections by electron impact for individual Pt and Au M subshells, which are scarce in the literature, particularly for Pt M_3, M_4, and M_5 subshells and for Au M_3 and M_4 subshells.

This approach is based on the measurement of x-ray-emission spectra induced by the incidence of an electron beam on thick targets, and their description, in terms of the ionization depth distribution function. Therefore, no thin specimen production is needed and the corresponding procedure for the film thickness determination is avoided.

The large dispersion of data for the fluorescence yields and the Coster-Kronig transition probabilities hampers the comparison between experimental values for the x-ray-production cross sections and those derived from theoretical or empirical models for the ionization cross sections. The difficulty inherent in the determination of such relaxation parameters suggests that a number of measurements for heavy elements and by means of different approaches is necessary to provide a reliable data set of x-ray-production cross sections for individual M subshells. This will enable the validation of different experimental procedures and theoretical models.

ACKNOWLEDGMENTS

This work was financially supported by the Secretaría de Ciencia y Técnica of the Universidad Nacional de Córdoba (UNC), Argentina. The authors are also grateful to the Laboratorio de Microscopía y Análisis por Rayos X (LAMARX-UNC), where the experimental determinations were performed.

APPENDIX: ASSESSMENT OF THE CHARACTERISTIC INTENSITY

The characteristic intensities emerging from a semi-infinite flat material under monoenergetic electron irradiation normal

to the surface can be expressed in terms of the ionization depth distribution function

$$\varphi(\rho z) = \frac{dn(\rho z)}{dn_o}, \tag{A1}$$

where $dn(\rho z)$ is the number of ionizations produced by the incident beam in an infinitesimal layer of mass thickness $d(\rho z)$ at depth z, and dn_o is the number of ionizations generated in an isolated identical layer irradiated with the same beam energy E_o. From the definition of the ionization cross section $\sigma_\ell(E_o)$ [50], the number of ionizations dn_o is the product of $\sigma_\ell(E_o)$ and the number of atoms per unit area in the layer $d(\rho z)$:

$$dn_o = \sigma_\ell(E_o)\frac{N_A}{A}\, d(\rho z), \tag{A2}$$

where N_A is Avogadro's number and A is the atomic weight.

By integration of Eq. (A1) along a semi-infinite sample, the primary detected characteristic intensity of the q line can be expressed as

$$P_q^1 = N_e\, \varepsilon(E_q)\, p_q\, \sigma_\ell^x(E_o)\frac{N_A}{A}\int_0^\infty d(\rho z)\, \varphi_q(\rho z) e^{-\xi_q \rho z}, \tag{A3}$$

where the exponential accounts for x-ray attenuation, $\xi_q = \mu_q\, \mathrm{cosec}(\psi)$, μ_q is the sample mass attenuation coefficient for photons of energy E_q, and ψ is the takeoff angle. Omitting the subindex q for simplicity, the total detected characteristic intensity can be written as

$$P = P^1 F, \tag{A4}$$

where F accounts for the fluorescence enhancement and is assessed following Reed [51]. Bearing in mind that the integral in Eq. (A3) involves the x-ray generation and its attenuation in the way to the sample surface, a ZA factor can be defined as

$$ZA = \frac{N_A}{A}\int_0^\infty d(\rho z)\varphi(\rho z) e^{-\xi\, \rho z}. \tag{A5}$$

To assess this expression, the model for $\varphi(\rho z)$ given by Packwood and Brown [52] was chosen, resulting in

$$ZA = \frac{\sqrt{\pi}}{2\alpha}\left[\gamma\, R\left(\frac{\xi}{2\alpha}\right) + (\gamma - \varphi_o)\, R\left(\frac{\beta+\xi}{2\alpha}\right)\right], \tag{A6}$$

where the parameters α, γ, φ_o, and β were assessed according to the models proposed by Riveros and Castellano [26]. The fifth-order polynomial R [53] allows us to provide a good estimate for the complementary error function arising when solving the integral involved in Eq. (A6). From these expressions, Eq. (2) can readily be assessed.

[1] F. Salvat, J. Fernández-Varea, and J. Sempau, *PENELOPE 2011: A Code System for Monte Carlo Simulation of Electron and Photon Transport* (OECD Nuclear Energy Agency, Issy les Moulineau, France, 2011).

[2] J. Trincavelli, S. Limandri, and R. Bonetto, Spectrochim. Acta, Part B **101**, 76 (2014).

[3] Z. Li and U. Becker, J. Electron Spectrosc. Relat. Phenom. **237**, 146893 (2019).

[4] A. Shornikov and F. Wenander, J. Instrum. **11**, T04001 (2016).

[5] M. Gryzinski, Phys. Rev. **138**, A336 (1965).

[6] J. Scofield, Phys. Rev. A **18**, 963 (1978).

[7] D. Bote, F. Salvat, A. Jablonski, and C. Powell, At. Data Nucl. Data Tables **95**, 871 (2009).

[8] S. Segui, M. Dingfelder, and F. Salvat, Phys. Rev. A **67**, 062710 (2003).

[9] C. Merlet, X. Llovet, and F. Salvat, Phys. Rev. A **78**, 022704 (2008).

[10] K. Ishii, M. Kamiya, K. Sera, S. Morita, H. Tawara, M. Oyamada, and T. C. Chu, Phys. Rev. A **15**, 906 (1977).

[11] D. H. H. Hoffmann, C. Brendel, H. Genz, W. Löw, S. Müller, and A. Richter, Z. Phys. A: At. Nucl. **293**, 187 (1979).

[12] H. Berndt and H.-J. Hunger, Phys. Status Solidi A **84**, K149 (1984).

[13] K. Murata and K. Sugiyama, J. Appl. Phys **66**, 4456 (1989).

[14] X. Llovet, C. Merlet, J. M. Fernández-Varea, and F. Salvat, Microchim. Acta **132**, 163 (2000).

[15] A. Moy, C. Merlet, X. Llovet, and O. Dugne, J. Phys. B: At., Mol. Opt. Phys. **46**, 115202 (2013).

[16] A. Moy, C. Merlet, and O. Dugne, Chem. Phys. **440**, 18 (2014).

[17] A. Moy, C. Merlet, X. Llovet, and O. Dugne, J. Phys. B: At., Mol. Opt. Phys. **47**, 055202 (2014).

[18] Z. An and Q. Hou, Phys. Rev. A **77**, 042702 (2008).

[19] P. D. Pérez, A. Sepúlveda, G. Castellano, and J. Trincavelli, Phys. Rev. A **92**, 062708 (2015).

[20] R. Bonetto, G. Castellano, and J. Trincavelli, X-Ray Spectrom. **30**, 313 (2001).

[21] S. Limandri, J. Trincavelli, R. Bonetto, and A. Carreras, Phys. Rev. A **78**, 022518 (2008).

[22] S. Limandri, A. Carreras, R. Bonetto, and J. Trincavelli, Phys. Rev. A **81**, 012504 (2010).

[23] S. Limandri, R. Bonetto, A. Carreras, and J. Trincavelli, Phys. Rev. A **82**, 032505 (2010).

[24] P. D. Pérez, A. C. Carreras, and J. C. Trincavelli, J. Phys. B: At., Mol. Opt. Phys. **45**, 025004 (2012).

[25] T. Rodríguez, A. Sepúlveda, A. Carreras, G. Castellano, and J. Trincavelli, J. Anal. At. Spectrom. **31**, 780 (2016).

[26] J. A. Riveros and G. E. Castellano, X-Ray Spectrom. **22**, 3 (1993).

[27] G. Castellano, J. Osán, and J. Trincavelli, Spectrochim. Acta, Part B **59**, 313 (2004).

[28] V. Scott, G. Love, and S. Reed, *Quantitative Electron-Probe Microanalysis*, 2nd ed. (Horwood, London, 1995), pp. 40–41 .

[29] J. Trincavelli, S. Limandri, A. Carreras, and R. Bonetto, Microsc. Microanal. **14**, 306 (2008).

[30] Moxtek, Inc., AP3 Datasheet, AP Window Mounts Note, https://moxtek.com/wp-content/uploads/WIN-DATA-1001-AP3-Ultra-thin-Windows-Rev-F.pdf; https://moxtek.com/wp-content/uploads/pdfs/Ultra-thin-AP3-Window-Mounts-WIN-TECH-1003-REV-B.pdf (accessed June 8, 2020).

[31] X. Llovet, C. Powell, F. Salvat, and A. Jablonski, J. Phys. Chem. Ref. Data **43**, 013102 (2014).

[32] C. Visñovezky, S. Limandri, M. E. Canafoglia, R. Bonetto, and J. Trincavelli, Spectrochim. Acta, Part B. **62**, 492 (2007).

[33] S. Limandri, A. Carreras, and J. Trincavelli, Microsc. Microanal. **16**, 583 (2010).
[34] W. Duane and F. Hunt, Phys. Rev. **6**, 166 (1915).
[35] J. Trincavelli, H. Andrada, and A. Carreras, J. Phys. B: At., Mol. Opt. Phys. **52**, 035003 (2019).
[36] P. J. Statham, X-Ray Spectrom. **6**, 94 (1977).
[37] R. D. Bonetto, A. C. Carreras, J. C. Trincavelli, and G. E. Castellano, J. Phys. B **37**, 1477 (2004).
[38] S. T. Perkins, D. E. Cullen, M. H. Chen, J. H. Hubbell, J. Rathkopf, and J. H. Scofield, Lawrence Livermore National Laboratory Report UCRL-50400 30, 1, 1991.
[39] O. Söğüt, E. Büyükkasap, A. Küçükönder, M. Ertuğrul, O. Doğan, H. Erdoğan, and O. Şimşek, X-Ray Spectrom. **31**, 62 (2002).
[40] Y. Chauhan and S. Puri, At. Data Nucl. Data Tables **94**, 38 (2008).
[41] M. Chen, B. Crasemann, and H. Mark, Phys. Rev. A **21**, 449 (1980).
[42] M. Chen, B. Crasemann, and H. Mark, Phys. Rev. A **27**, 2989 (1983).
[43] G. Kaur and R. Mittal, J. Quant. Spectrosc. Radiat. Transfer **133**, 489 (2014).
[44] E. McGuire, Phys. Rev. A **5**, 1043 (1972).
[45] D. Bote and F. Salvat, Phys. Rev. A **77**, 042701 (2008).
[46] E. Casnati, A. Tartari, and C. Baraldi, J. Phys. B: At. Mol. Phys. **15**, 155 (1982).
[47] C. Merlet, in *Proceedings of the 29th Annual Conference of the Microbeam Analysis Society*, edited by E. Etz (VCH, New York, 1995), pp. 203–204.
[48] X. Llovet and C. Merlet, Microsc. Microanal. **16**, 21 (2010).
[49] C. Merlet, Microchim. Acta Suppl. **12**, 107 (1992).
[50] J. Goldstein, D. Newbury, J. Michael, N. Ritchie, J. Scott, and D. Joy, *Scanning Electron Microscopy and X-Ray Microanalysis*, 4th ed. (Springer, New York, 2017), p. 46.
[51] S. Reed, Br. J. Appl. Phys. **16**, 913 (1965).
[52] R. Packwood and J. Brown, X-Ray Spectrom. **10**, 138 (1981).
[53] M. Abramowitz and I. Stegun, *Handbook of Mathematical Functions*, 9th ed. (Dover, New York, 1970), p. 299.